Building and Environment 195 (2021) 107729

Contents lists available at ScienceDirect

Building and Environment

journal homepage: http://www.elsevier.com/locate/buildenv

A cooled city? Comparing human activity changes on the impact of urban thermal environment before and after city-wide lockdown

Zhi Cai [a], Yan Tang [a,*], Qingming Zhan [b]

[a] School of Architecture, Tsinghua University, Beijing, 100084, China
[b] School of Urban Design, Wuhan University, Wuhan, 430072, China

ARTICLE INFO

Keywords:
COVID-19
Thermal environment
Human activity
Anthropogenic heat
Urban land use
LCZ

ABSTRACT

The outbreak of the COVID-19 epidemic in early 2020 reduced human outdoor activities and changed the spatial-temporal distribution of the population. To find its changes on the impact of urban thermal environment, we applied Pearson correlation analysis and OLS linear regression model from the perspective of urban land use and the local climate zone (LCZ) scheme, and selected Wuhan City in China as a case study. The results showed that the population size decreased in most urban land use and LCZ classes due to the Spring Festival and epidemic effects, which caused residents to leave Wuhan City. As a result, the normalized surface urban heat island changes ($SUHI_{nc}$) decreased by 9.41% at the city level, and a larger $SUHI_{nc}$ occurred in commercial and industrial land. Among the LCZ classes, the built-up classes also tended to have a larger $SUHI_{nc}$ than the natural land cover classes. However, the population size and human outdoor activity changes did not modify the spatial distribution of the urban thermal environment, because the same trends were observed for various urban land use and LCZ classes, which illustrated that the contribution of anthropogenic heat discharge on the urban thermal environment is relatively weaker. The above findings imply that it is necessary to apply different methods for various urban land uses and alleviate urban heat island.

1. Introduction

COVID-19 has changed our daily life. To limit the spread of the COVID-19 pandemic, most countries closed their borders, locked down their cities, and confined residents to their homes. Therefore, human outdoor activities, such as transportation, shopping and traveling, were reduced [1]. Numerous factories were also closed due to the epidemic effect. These changes caused less energy consumption for cities during the lockdown period than on normal workdays [2], which reduced CO_2 emissions and anthropogenic heat release [3]. Meanwhile, the outbreak of COVID-19 combined with the Chinese lunar new year (Spring Festival), above 30% of residents went back to their home town for Spring Festival, making big changes in population size and human activity in some Chinese cities. According to the surface energy balance (SEB) [4–7] (Fig. 1), anthropogenic heat released by human activities (e.g. human metabolism, building energy consumptions and vehicle traffic emissions) and solar radiation from the sun represents the two major sources of urban heat [8]. However, solar radiation regularly changes with the season and shows little difference under similar weather conditions. Physically, the retrieved land surface temperature (LST) from remote sensing satellite images can be regarded as the following function of SEB components [5]:

$$LST = f(R_n,\ A,\ G,\ LE,\ and\ H) \tag{1}$$

Therefore, the changes in human activities caused by COVID-19 and Spring Festival are expected to impact the urban thermal environment, as some previous studies have shown that anthropogenic heat release can increase the urban temperature by several degrees [9,10].

In addition to heat sources, the urban thermal environment is influenced by many factors, such as the climate zone [11,12], urban physical characteristics (e.g., urban spatial form, land cover, roof, and building materials) [13–19], socioeconomic factors (e.g., land use, energy consumption, and economic level) and population characteristics (e.g., size, age, and income) [13,20–23]. Of those factors, urban physical characteristics determined the level of solar radiation received by the land surface and converted to sensible heat. Indicators such as the Normalized Difference Built-up Index (NDBI), Normalized Difference Vegetation Index (NDVI) can be calculated by using remote sensing images, and quickly assessing the contribution of solar radiation to the urban thermal environment. Moreover, urban design methods based on

* Corresponding author.
E-mail addresses: czhi0911@gmail.com (Z. Cai), yantang@mail.tsinghua.edu.cn (Y. Tang), qmzhan@whu.edu.cn (Q. Zhan).

https://doi.org/10.1016/j.buildenv.2021.107729
Received 1 December 2020; Received in revised form 20 January 2021; Accepted 15 February 2021
Available online 23 February 2021
0360-1323/© 2021 Elsevier Ltd. All rights reserved.

urban physical characteristics are the most effective way to improve the urban thermal environment [12,24], such as providing more green spaces or water bodies [25–27], optimizing the urban spatial form [28,29], designing cool pavements [18], and installation low albedo building materials [19]. Therefore, scholars have paid more attention to urban physical characteristics, and made remarkable achievements in studying urban thermal environments. Scholars have also proposed some useful methods to bridge urban physical characteristics and the urban thermal environment, such as the local climate zone scheme (LCZ) [30]. In recent years, scholars have broadened the scope of the LCZ and applied the LCZ to other issues, such as urban health [31], heat vulnerability and carbon emissions [21,32].

In contrast, studies focusing on the urban thermal environment from socioeconomic and population perspectives are limited [33,34]. Estimating the amount of anthropogenic heat release is difficult because of the lack of socioeconomic and population data. Moreover, the various socioeconomic status and population characteristics in different cities, which limit the suitability of thermal environment improvement methods to a specific city [35], such as social governance and government response [36,37]. Therefore, to fill this gap, some studies have begun using big data based on mobile users to explore the distribution of populations and their characteristics [38,39]. The enrichment of energy consumption data has also made it possible to estimate anthropogenic heat release by the inventory method [40]. Some climate models have also provided a window to assess the impact of human activities and their anthropogenic heat releases on the urban thermal environment, such as ENVI-met and WRF [41,42].

However, it should be noted that the inventory method cannot reflect the fine spatial distribution of anthropogenic heat release and does not refer to the urban thermal environment. In climate models, the study area is considered as an ideal virtual environment, the impact of populations and their anthropogenic heat release on the urban thermal environment is simulated at the site-level microscale. In a real built environment, it is difficult to detect big human activity changes in the daytime, and using climate models to simulating their impact on the urban thermal environment at the city-level mesoscale with a fine spatial resolution. Moreover, it still scatters studies that combine populations and their activities changes with the LCZ scheme and their interactions with the urban thermal environment. The outbreak of COVID-19 has decreased human activities and anthropogenic heat release, which provided an ideal experimental built environment and makes it possible to assess and compare the influences of human activities on the urban thermal environment. Therefore, in this paper, we addressed those issues from the perspective of urban land use and LCZ scheme, because urban land use is highly correlated with human activities [43,44], and LCZ characterizes urban morphology. Wuhan City in China was selected as a case study, which aims to find:

1) What is the impact of COVID-19 on human activities and population distributions?
2) Do the changes of human activities and population size redistribute the urban thermal environment?
3) What is an effective method of measuring the contribution of anthropogenic heat release to urban microclimate in a real built environment at mesoscale?

2. Data and methods

2.1. Study area

Wuhan is the capital city of Hubei Province in China, and it is located between 29°58′-31°22′ north latitude and 113°41′-115°05′ east longitude (Fig. 2). Wuhan has a subtropical monsoon climate. As one of the "stove cities" in China, its annual average air temperature ranges from 15.8 °C to 17.5 °C, and its highest air temperature can reach 40 °C on summer days. According to the Wuhan government census data, the permanent population reached 9.06 million and the floating population accounted for 5.1 million by the end of 2019 [45].

The outbreak of COVID-19 in Wuhan City caused a serious public health crisis. To limit the spread of the disease, the Chinese government placed Wuhan City under lockdown on January 23, 2020, and the lockdown was lifted on April 8, 2020 [46]. During the lockdown period, most of the outdoor activities stopped. Moreover, before the city-wide lockdown, more than 5 million residents returned to their hometowns for the Spring Festival. The epidemic effect combined with the Spring Festival made the city appear to be "empty" during the lockdown period.

2.2. Data sources and pre-processing

Cloud-free Landsat 8 remote sensing images with level 1 data were downloaded from the United States Geological Survey (USGS) website (http://earthexplorer.usgs.gov/), and these images were used to retrieve land surface temperature (LST). To reduce the influence of different weather conditions, we selected images acquired under similar

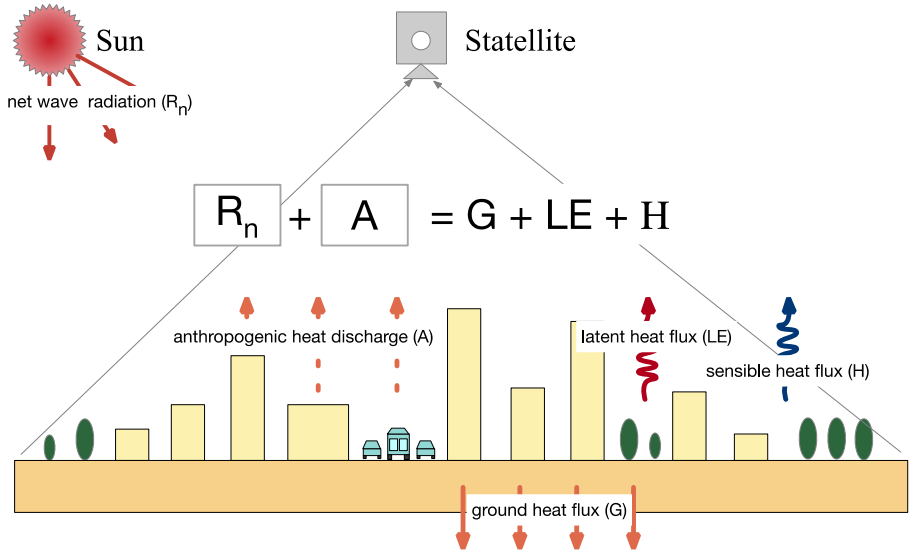


Fig. 1. The urban surface energy balance. (R_n, A, G, LE and H is the net wave radiation, anthropogenic heat discharge, ground heat flux, latent heat flux and sensible heat flux, respectively.)

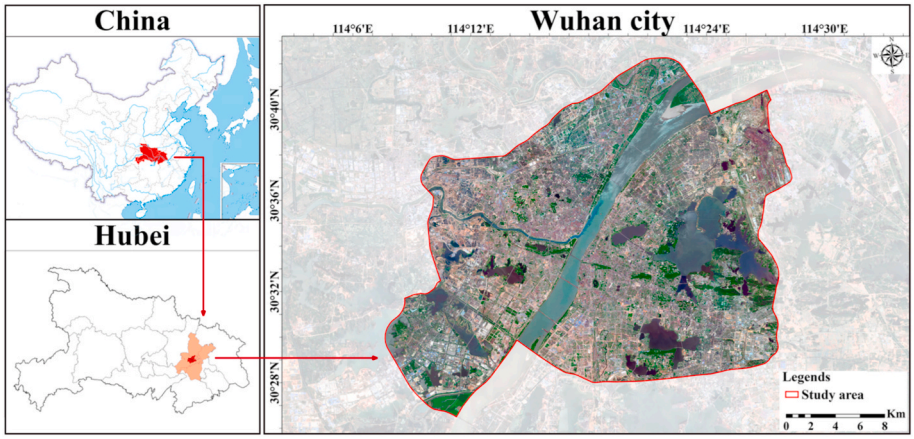


Fig. 2. Location of the study area.

weather conditions for comparison (Table 1). All of the images were acquired at 10:56 a.m. by satellite, with a path of 123 and a row of 39.

Urban land use information was collected from the local government (Fig. 4a), and the building information (e.g., floor, area and outline) was download from the Baidu map with an API tool. The Google satellite images with a 0.5 m spatial resolution were clipped from Google Maps. The real-time population distribution information was acquired three times per day (9:00, 11:00 and 21:00) by a Python code from EasyGo platform. EasyGo provides location servers for multiple mobile apps, such as WeChat, Meituan and QQ. Among them, WeChat has 1.2 billion active users worldwide, which covers over 70% of the Chinese population. Since EasyGo did not provide historical data, we used the data on June 4, 2020, to represent a normal workday's population distribution (Table 1). All of the data were imported to ArcGIS Pro software (version 2.6) for pre-processing, such as study area clipping and geometric correction.

2.3. Methods

2.3.1. Setting spatial cells

Many studies have found that the spatial scale influences the correlations between urban morphology indicators and LST [47,48], and they showed that the optimal spatial scale ranges from 300 m to 500 m in different cities. Since urban planning is based on land blocks, most of the land block lengths in Wuhan City ranges from 300 m to 500 m. Therefore, we set the land block as the spatial cells in this study (Fig. 3).

2.3.2. Land cover classification and calculation of the urban morphology index

Landsat 8 remote sensing images were used to calculate the NDVI, NDBI and Modified Normalized Difference Water Index (MNDWI). The NDVI was used to capture the green spaces, the NDBI was used to identify the impervious surfaces, and the MNDWI was used to classify water bodies. Google satellite images were used to delineate those classifications. The values of the NDVI, NDBI and MNDWI can be calculated as follows:

$$NDVI = \frac{NIR - R}{NIR + R} \tag{2}$$

$$NDBI = \frac{SWIR - NIR}{SWIR + NIR} \tag{3}$$

$$MNDWI = \frac{G - SWIR}{G + SWIR} \tag{4}$$

where NIR represents the near-infrared band (band 5), R represents the red band (band 4), SWIR represents the shortwave-infrared band (band 6), and G represents the green band (band 3).

The building information was used to calculate the BD and mean building height (MH) for every land block. BD and MH can be calculated using the following equations:

$$BD = \frac{\sum_{i=1}^{N} C_i}{C_B} \tag{5}$$

$$MH = \frac{\sum_{i=1}^{N} C_i H_i}{\sum_{i=1}^{N} C_i} \tag{6}$$

$$PD = \frac{P_B}{C_B} \tag{7}$$

$$PD_c = \frac{PD_L - PD_W}{PD_W} \times 100\% \tag{8}$$

where N is the number of buildings located in a land block, C_i is the coverage area of the building, C_B is the area of the land block, H_i is the building height; PD is the population density in a land block, P_B is the total population number dispersed in a land block, PD_c represents the population changes after the city lockdown, PD_L and PD_W are the population densities during lockdown periods and workdays, respectively. To accurately capture the distribution of populations, the average population size per day was calculated and used in this study.

2.3.3. LCZ classification

The LCZ scheme classified the urban areas into built-up and land cover types, which identified 17 different classes [29]. Ten are built-up types (LCZ 1–10), and seven are land cover types (LCZ A-G) (Table 2). The LCZ scheme has also offered some standard urban morphology indicators and their values for classification, such as the BD, impervious surface fraction (ISF) and pervious surface fraction (PSF) (Tab A.1). Studies have also shown that the LCZ scheme and its indicators can be applied worldwide [49,50]. Therefore, in this study, we selected the BD,

Table 1
Data acquisition time and local weather conditions.

	Remote sensing images	Air temperature (°C)	Wind speed (m/s)	Period	Population data
Comparison 1	2019/12/07	0–14	0.3–1.5	Workday	2020/06/04
	2020/02/09	0–14	0.3–1.5	Lockdown	2020/02/29
Comparison 2	2018/04/08	10–23	1.6–3.3	Workday	–
	2020/04/13	11–23	1.6–3.3	Post-lockdown	2020/04/13



Fig. 3. Spatial scale based on the land block (a sample for the study area).

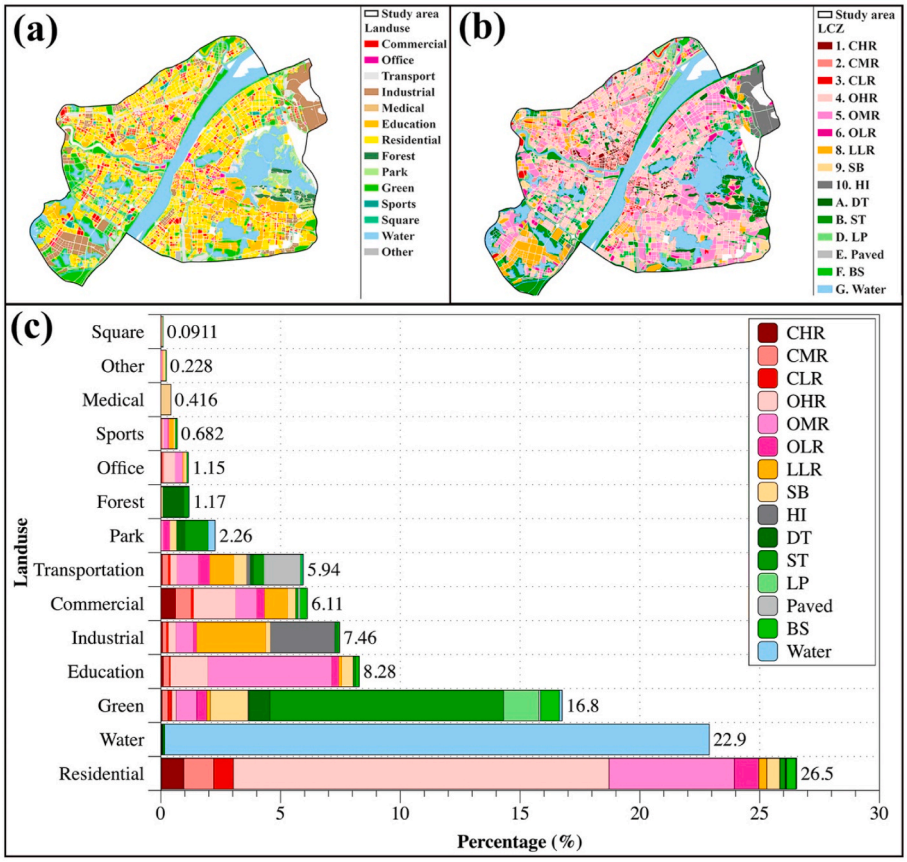


Fig. 4. Distribution of urban land use (a) and LCZ classes (b), the percentage of urban land use area and its LCZ class composition in the study area (c).

MH, ISF and PSF for LCZ classification. The classified results are shown in Fig. 4b.

2.3.4. LST retrieval

The LST toolbox in Arcgis provided by Sekertekin et al. [51] is used to retrieve LST, and the Radiative transfer equation method is selected, which is based on the following equation:

$$L_{sensor} = [\varepsilon B_{\lambda}(T_S) + (1-\varepsilon)L\downarrow]\tau + \quad L\uparrow \tag{9}$$

where L_{sensor} is the radiation intensity ($W{\cdot}m^{-2}{\cdot}sr^{-1}\ \mu m^{-1}$) received by

Table 2
LCZ scheme.

Built-up classes			Land cover classes		
LCZ classes	Full name	Abbreviation	LCZ classes	Full name	Abbreviation
LCZ 1	Compact high-rise	CHR	A	Dense trees	DT
LCZ 2	Compact mid-rise	CMR	B	Scattered trees	ST
LCZ 3	Compact low-rise	CLR	C	Bush, scrub	–
LCZ 4	Open high-rise	OHR	D	Low plants	LP
LCZ 5	Open mid-rise	OMR	E	Bare rock or paved	Paved
LCZ 6	Open low-rise	OLR	F	Bare soil or sand	BS
LCZ 7	Lightweight Low-rise	–	G	Water	Water
LCZ 8	Large low-rise	LLR			
LCZ 9	Sparsely built	SB			
LCZ 10	Heavy industry	HI			

the remote sensing of related thermal band (band 10), L↓ represents the atmospheric downwelling path radiance, L↑ represents the upwelling path radiance, and τ represents atmospheric transmissivity. L↓, L↑ and τ can be obtained from the NASA website (http://atmcorr.gsfc.nasa.gov/). $B_\lambda(T_S)$ is the ground radiance; according to Plank's law, $B_\lambda(T_S)$ can be expressed as the following equation:

$$B_\lambda(T_S) = \frac{2hc^2}{\lambda^5} \times \frac{1}{e^{\frac{hc}{\lambda k T_S}} - 1} \tag{10}$$

where T_s is the land surface temperature in Kelvin, h is the Planck constant (6.6261×10^{-34} J s), c is the light speed (2.9979×10^{8} m/s), λ is the band wavelength, k is the Boltzmann constant (1.3806×10^{-23} J/K). Thus, T_S can be obtained from Eqs. (9) and (10) and expressed as follows:

$$T_S = \frac{K_2}{\ln\left(\frac{K_1}{L_{sensor} - L\uparrow - \tau(1-\varepsilon)L\downarrow/\tau\varepsilon} + 1\right)} \tag{11}$$

For the Landsat 8 TIRS Band 10 data, $K_1 = 774.89$ W m^{-2}·sr^{-1}·μm^{-1} and $K_2 = 1321.08$ K ε represents the land surface emissivity, its value can be estimated from NDVI threshold-based model [52]:

$$\varepsilon = \begin{cases} 0.979 - 0.046\rho_R & NDVI < 0.2 \\ 0.987 P_V + 0.971\,(1 - P_V) + d\varepsilon & 0.2 \le NDVI \le 0.5 \\ 0.987 + d\varepsilon & NDVI > 0.5 \end{cases} \tag{12}$$

where ρ_R is the reflectance value of the red band, dε is the cavity effect and regarded as 0 for flat surfaces, P_v is the vegetation fraction and can be calculated as follows:

$$P_V = \left[\frac{NDVI - NDVI_{min}}{NDVI_{max} - NDVI_{min}}\right]^2 \tag{13}$$

where $NDVI_{min} = 0.2$, $NDVI_{max} = 0.5$.

The land surface temperature in Centigrade can be expressed as:

$$LST = T_S - 273.15 \tag{14}$$

According to ground meteorological station data, the measured LST is 12.2 °C (workday), 13.0 °C (lockdown), and the retrieved LST is 11.78 °C, 12.45 °C, respectively. It illustrated that the retrieved LST is reliable.

2.3.5. SUHI and its changes

Since we used remote sensing images from different days for LST retrieval and LST ranges of different values, to further eliminate the influences of different weather conditions and made the thermal index comparable. Surface urban heat island (SUHI) was applied in this study. Its value is the surface temperature difference between the land block/LCZ classes and forestland/dense trees, which is also proposed by Stewart [29] in urban temperature studies. SUHI can be calculated as follows:

$$SUHI = LST_l - \overline{LST_f} \tag{15}$$

$$SUHI_n = \frac{SUHI - SUHI_{min}}{SUHI_{max} - SUHI_{min}} \tag{16}$$

$$SUHI_{nc} = \frac{SUHI_{nL} - SUHI_{nW}}{SUHI_{nW}} \times 100\% \tag{17}$$

where LST_l is the LST value of land block or LCZ classes, $\overline{LST_f}$ is the mean LST value of forestland or dense tress class. $SUHI_n$ is the normalized value of SUHI, its value ranges from 0 to 1. $SUHI_{min}$ and $SUHI_{max}$ represent the minimum and maximum SUHI values in the study area, respectively. $SUHI_{nc}$ is the normalized surface urban heat island changes before and after the city lockdown, $SUHI_{nL}$ and $SUHI_{nW}$ represent the $SUHI_n$ value during lockdown and workday, respectively.

2.3.6. Correlation analysis and regression analysis

Pearson correlation analysis was applied to determine the influence of population changes on the urban thermal environment, and the Pearson coefficients were compared for different urban land uses. The ordinary least squares (OLS) linear regression model was used in this study, which aims to assess and compare different factors and their changes in the contributions to urban thermal environment. The OLS model can be expressed as follows:

$$LST = a_0{*}NDBI + b_0{*}MNDWI + c_0{*}PD + d_0 \tag{18}$$

$$SUHI_{nc} = a_1{*}\Delta NDBI + b_1{*}\Delta MNDWI + c_1{*}PD_c + d_1 \tag{19}$$

where a_0, a_1, b_0, b_1, c_0 and c_1 are the coefficients of each factor, d_0 and d_1 is the error term. ΔNDBI and ΔMNDWI are the NDBI differences and MNDWI differences between the lockdown/post-lockdown and workday periods, respectively.

3. Results

3.1. Population distribution and its changes

The population has a similar spatial distribution before and after the city-wide lockdown (Fig. 5a, Fig. 5b and c), as the Pearson correlations between lockdown and workday period, post-lockdown and workday period reached 0.915** ($P < 0.01$), 0.965** ($P < 0.01$), respectively. Residential land has the highest population size, followed by commercial land, education land, and industrial land (Fig. 5d).

The COVID-19 epidemic had a big impact on human activities and population changes in different urban land uses (Fig. 5d). Combined with the Spring Festival and the influence of COVID-19, numerous residents left Wuhan City, which caused the population size to decrease by 33.99% compared with normal workdays at the city level. The population size among all urban land uses has decreased. In urban construction lands, the percentages of the population decreased in the areas of industrial (−82.46%), commercial (−70.35%), medical (−62.82%), transportation (−62.45%), office (−60.04%), education (−52.37%), and residential (−27.64%) (Fig. 5c). In open spaces and natural cover lands, the percentages of population decreased in the areas of square (−85.11%), park (−60.82%), green (−58.22%), forest (−54.69%) and water (−53.79%).

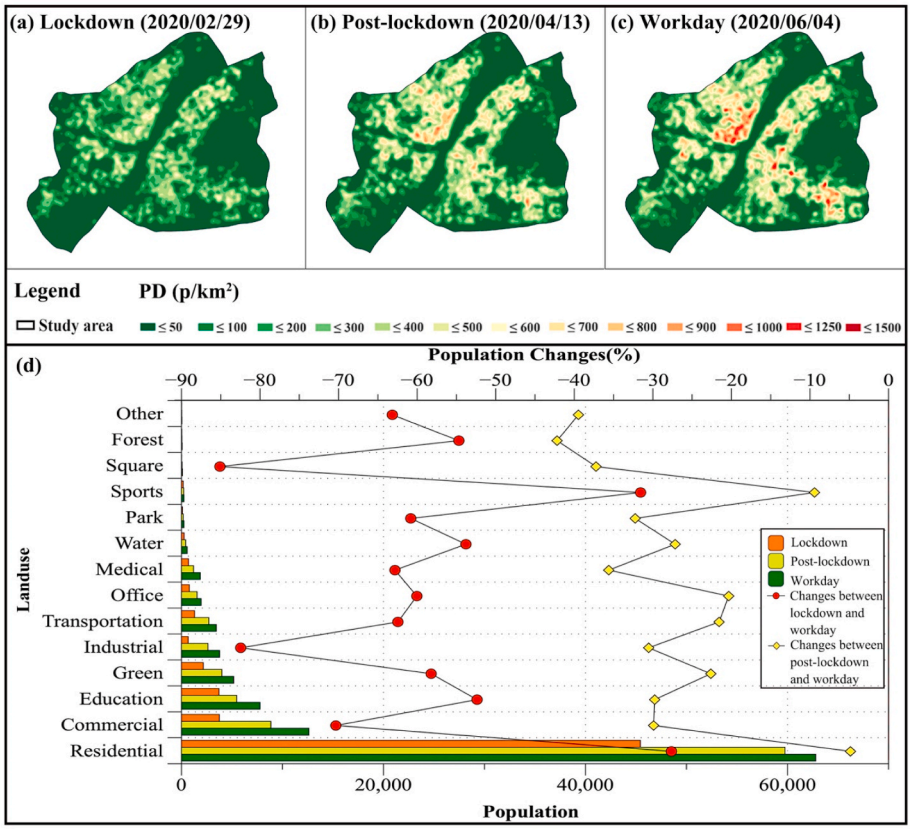


Fig. 5. Spatial distribution of the population during lockdown period (a), post-lockdown period (b) and normal workday (c); population distribution of different urban land uses and its changes after the city lockdown (d).

Since the city-wide lockdown, most factories shut down to cut the epidemic spread, restaurants and shop stores also closed. Therefore, the human activities in those lands (industrial and commercial) were heavily influenced by the epidemic and reduced its population size. For medical land, residents were concerned about being infected at the hospital [53], and the local government did not encourage them to go to the hospital; thus, most people were diagnosed or searched for help through online platforms [54,55]. Moreover, to reduce the infection risk, the hospitals mainly served COVID-19 patients, which reduced the population size for this land use in the epidemic period. For transportation and office land, several departments and facilities were still running during the epidemic period, such as the local government. Therefore, some populations were still present on those land types, which led to a moderate population decrease. For residential land, although numerous residents did not work outside and stayed at home, it should be noted that approximately 35% of the residents returned to their hometown for the Spring Festival, which reduced the impact of COVID-19 on residential land. Therefore, minimum population changes were observed. For open spaces and natural cover lands, most of the outdoor activities disappeared in the epidemic period, which could have produced a big population change before and after the city-wide lockdown. Since the lockdown was lifted on April 8, some residents have gone back to Wuhan City, urban public facilities and factories have gradually opened up, which caused the population differences to slightly decrease in the post-lockdown period when compared to a normal workday.

3.2. LST distribution and its changes

The LST shows a similar spatial distribution and the same trend in various urban land uses before and after the city lockdown (Fig. 6a). In urban construction lands, industrial land has the highest LST, followed by sports, transportation, education, commercial, medical, office and residential land, and this finding was generally consistent with previous studies [16,56]. Open spaces and natural cover land types tend to have a lower LST and decrease in the order of green land, square land, water bodies, parkland and forest land (Fig. 6a). Industrial land has little green space, and its buildings are large low-rise with dark or metal roofs. These buildings easily absorb solar energy and transform them into sensible heat, thus producing a high LST. For sports and education land, sports grounds with impervious surfaces and dark colors cover many areas and produce a higher LST. Commercial and office land is always located in the city centre, which has dense high-rise buildings and few trees, thus leading to a worse thermal environment. However, the tall buildings in the city centre can provide many building shadows, reduce solar radiation reaching the surface, and decrease LST. Residential land has numerous green spaces and high-rise buildings, some of them are also near water bodies. The cooling effect of green spaces and water bodies combined with building shadows can make residential land have a lower LST. For open spaces (park and forest), the large percentage of pervious surfaces can reflect much of the solar energy and less anthropogenic heat release occurs, which can produce the lowest LST.

The changes in population size caused by the COVID-19 epidemic and Spring Festival still had an impact on the urban thermal environment. As the SUHI effect decreased in most urban land uses during the lockdown period compared with normal workdays (Fig. 6b), and big $SUHI_{nc}$ were observed in different urban land uses (Fig. 6c). After the city lockdown, the $SUHI_{nc}$ decreased by 9.41% at the city level and thermal changes were decreased as following orders: commercial (−11.08%), residential (−10.75%), education (−10.62%), square (−9.72%) and industrial lands (−9.52%). Since shopping and manufacturing activities are heavily influenced by the epidemic and those activities also release tremendous anthropogenic heat, commercial and industrial land had the highest thermal environment differences.

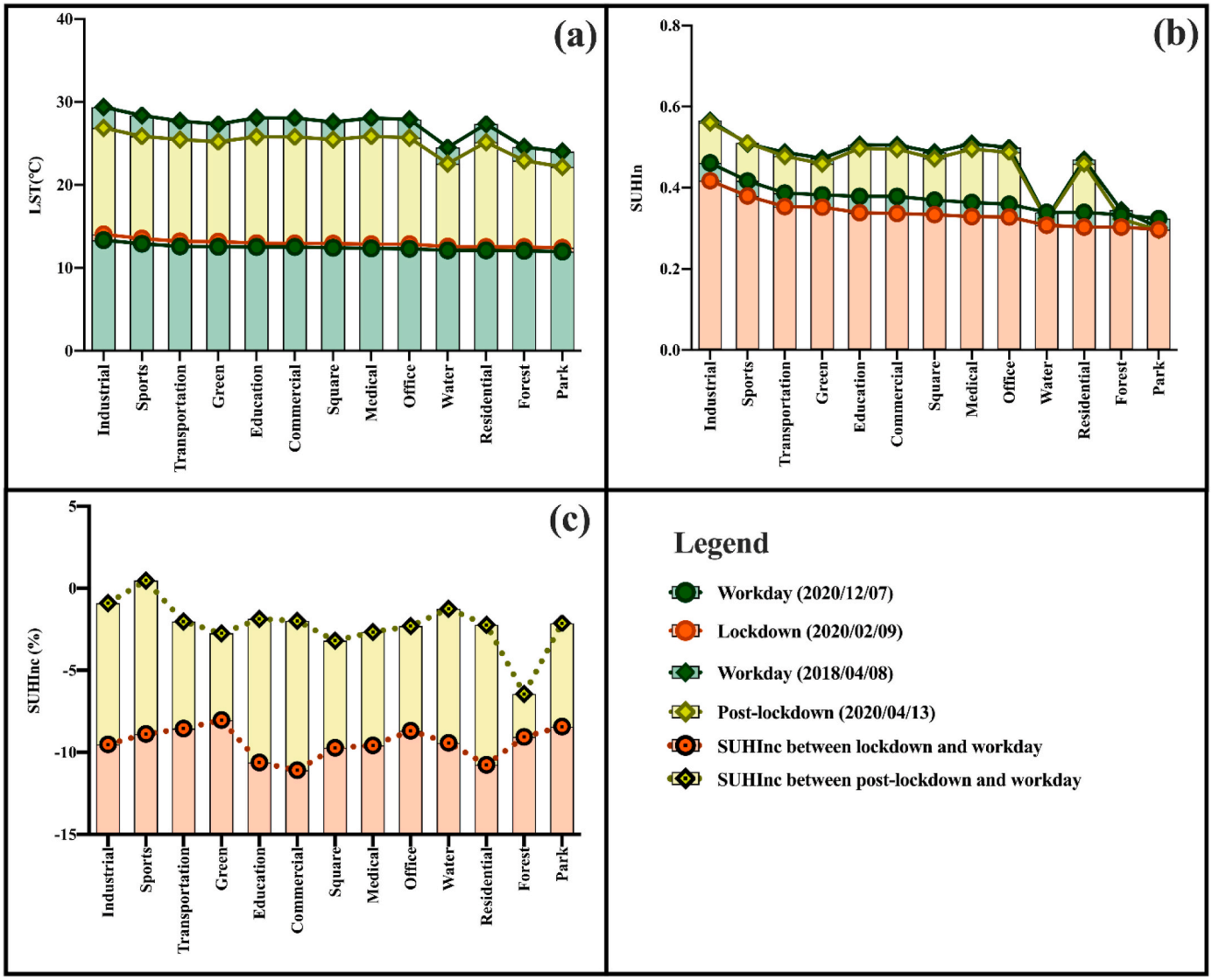


Fig. 6. Land surface temperature (LST) (a), Normalized surface urban heat island (SUHIn) (b), and normalized surface urban heat island changes (SUHInc) for various urban land uses (c).

Although small population change percentages were observed for residential and educational lands (Fig. 5d), those areas have large populations that decreased by several million residents due to the Spring Festival. This population decline can also decrease the total amount of anthropogenic heat released and produce a big thermal difference. Only a few residents live in the open spaces, these lands mainly receive energy from solar radiation; thus, limited differences were observed in their thermal environment.

In the post-lockdown period, the outdoor and working activities gradually returned to normal life. However, they did not reach a normal level; thus, the urban land use still had a lower $SUHI_n$ compared with the normal workday (Fig. 6b) and showed slight thermal differences between the post-lockdown and workday period (Fig. 6c).

3.3. Correlations between population changes and urban thermal environment changes

To further determine the impact of COVID-19 and the Spring Festival on the urban thermal environment, we applied a correlation analysis. The results showed that the PD_c had a positive relationship with the $SUHI_{nc}$ for most urban land uses, with a significant positive relationship (0.145**, $P < 0.01$) observed at the city level (Fig. 7c). In urban

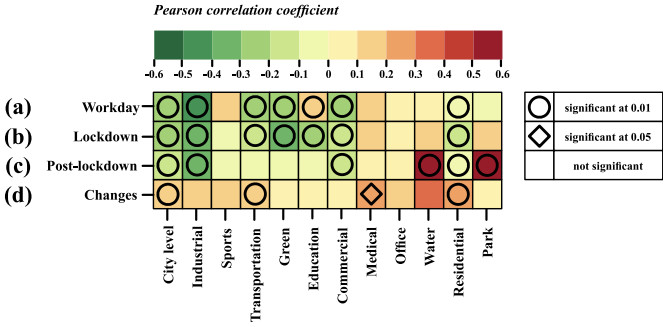


Fig. 7. Pearson coefficient between PD and LST on workdays (a), lockdown (b) and post-lockdown periods (c); Pearson coefficient between population density changes (PD_c) and normalized surface urban heat island changes ($SUHI_{nc}$) (d).

construction lands, a significant relationship was only observed in transportation (0.198**, $P < 0.01$), medical (0.205*, $P < 0.05$) and residential lands (0.231**, $P < 0.01$). In other lands, the PD_c did not have a significant relationship with $SUHI_{nc}$, with the coefficients decreasing in the order of industrial (0.135), office (0.117), commercial

(0.067) and education (0.057). Since a few populations were located in open spaces and natural cover lands, the changes of anthropogenic heat release had little impact on the urban thermal environment and caused a weak and non-significant relationship between the PD_c and $SUHI_{nc}$ in those lands.

The OLS regression model showed that the population and its associated activities changes are the major drivers underlying urban thermal differences in similar weather conditions. Because of the big population changes between the lockdown and workday periods (Fig. 5d), the PDc had the highest absolute standardized coefficient beta value compared with the ΔNDBI and ΔMNDWI (Table 3-Model 4). With a smaller population change between the post-lockdown and workday periods, the PDc had a limited effect on the urban thermal differences and the regression model was no longer stable (Table 3-Model 5).

4. Discussions

4.1. Comparing the contributions of population and land cover to the urban thermal environment

Although big population size changes and thermal differences were observed before and after the city lockdown, the LST showed the same trend for various urban land uses in different periods (Fig. 6). This finding implies that other factors play an essential role in the urban thermal environment, such as land cover and urban morphology.

To further identify this hypothesis, we applied an OLS regression analysis with PD and land cover indicators (NDBI and MNDWI). Due to the anthropogenic heat release depends on the population size and its activities, and the solar radiation converted to sensible heat depends on the land cover, urban morphology and albedo [6]. The results showed that the land cover index has a greater contribution to the LST than the PD for the workday, lockdown and post-lockdown periods, which was shown by decrease in the absolute standardized coefficient beta values from the MNDWI to NDBI and PD (Table 3). The MNDWI captures water bodies and building shadows. Wuhan City has numerous water bodies and tall buildings, which results in a significant negative relationship between MNDWI and LST. The NDBI reflects the conditions of impervious surfaces, such as building surfaces and paved roads, and its significant positive contribution to LST has been identified by many studies [57,58]. Since the energy of anthropogenic heat release is only equal to 12% of solar radiation [7], it only increases the average surface temperature by 0.83 K in winter [59], which results in a weak contribution of the population to LST.

4.2. Comparing the population and thermal environment changes from the perspective of the LCZ

Since the urban morphology or land cover plays a more important role in the urban thermal environment, we have also analysed the population and thermal environment changes from the perspective of the LCZ. The results showed that most populations are located in built-up classes and the population size has decreased in all of the LCZ classes after the city-wide lockdown (Fig. 8a). The larger percentage of the population decreased appeared in the BS, LLR and HI classes, and it decreased slightly in other classes, such as OHR, OMR and CLR (Fig. 8a). BS represents open space in urban areas, the LLR and HI classes represent industrial land in urban land use, and the human activities on those lands have been heavily influenced by the epidemic, which caused big population changes before and after the city-wide lockdown. The OHR, OMR and CLR classes were more likely to appear in residential land (Fig. 4c); because the epidemic had less of an impact on residential activities, the percentage of population has little change in these LCZ classes.

The thermal environment showed a same trend in various LCZ classes before and after the city-wide lockdown, and the built-up classes tended to have larger thermal environment difference than the land cover classes after the lockdown. HI and LLR had the highest LST. Compact classes (CLR, CMR and CHR) tended to have a higher LST than open classes (OLR, OMR and OHR), and low-rise classes (OLR, CLR) tended to have a higher LST than mid-rise (OMR, CMR) and high-rise classes (OHR, CHR) (Fig. 8b), which is consistent with previous studies [49,60]. Since the epidemic and Spring Festival heavily influence human activities and population size in the built-up classes, the built-up classes tended to have a higher $SUHI_{nc}$ than the land cover classes. The $SUHI_{nc}$ decreased in the order of CHR (−13.76%), CLR (−10.92%), CMR (−10.56%), OHR (−10.54%), HI (−10.12%), OMR

Table 3
OLS linear regression model results for LST in the workday (Model 1), lockdown (Model 2) and post-lockdown (Model 3) periods, OLS linear regression model for $SUHI_{nc}$ between the lockdown and workday periods (Model 4) and between the post-lockdown and workday periods (Model 5).

Model 1	Workday				Model 2	Lockdown			
$R^2 = 0.455$	Unstandardized B	Standardized Coefficients Beta	t	Sig.	$R^2 = 0.455$	Unstandardized B	Standardized Coefficients Beta	t	Sig.
(Constant)	13.138		470.92	0.00	(Constant)	13.144		372.54	0.00
NDBI	7.860	0.222	16.563	0.00	NDBI	6.842	0.177	11.188	0.00
MNDWI	−11.192	−0.490	−34.657	0.00	MNDWI	−13.894	−0.514	−31.058	0.00
PD	−167.556	−0.063	−5.924	0.035	PD	−566.561	−0.102	−8.037	0.00
Dependent variable: LST					Dependent variable: LST				
Model 3	Post-lockdown				**Model 4**	**Comparison between lockdown and workday**			
$R^2 = 0.427$	Unstandardized B	Standardized Coefficients Beta	t	Sig.	$R^2 = 0.121$	Unstandardized B	Standardized Coefficients Beta	t	Sig.
(Constant)	27.965		382.62	0.00	(Constant)	0.055		41.829	0.00
NDBI	16.555	0.467	38.536	0.00	ΔNDBI	−0.152	−0.039	−2.176	0.03
MNDWI	−11.427	−0.297	−22.595	0.00	ΔMNDWI	16.518	0.133	8.645	0.00
PD	−672.14	−0.114	−10.303	0.00	PDc	0.700	0.291	16.071	0.00
Dependent variable: LST					Dependent variable: SUHInc				

Model 5	**Comparison between post-lockdown and workday**			
$R^2 = 0.004$	Unstandardized B	Standardized Coefficients Beta	T	Sig.
(Constant)	0.008		13.077	0.00
ΔNDBI	0.102	0.066	3.979	0.00
ΔMNDWI	0.023	0.013	0.816	0.414
PDc	−2.975	−0.019	−1.303	0.193
Dependent variable: SUHInc				

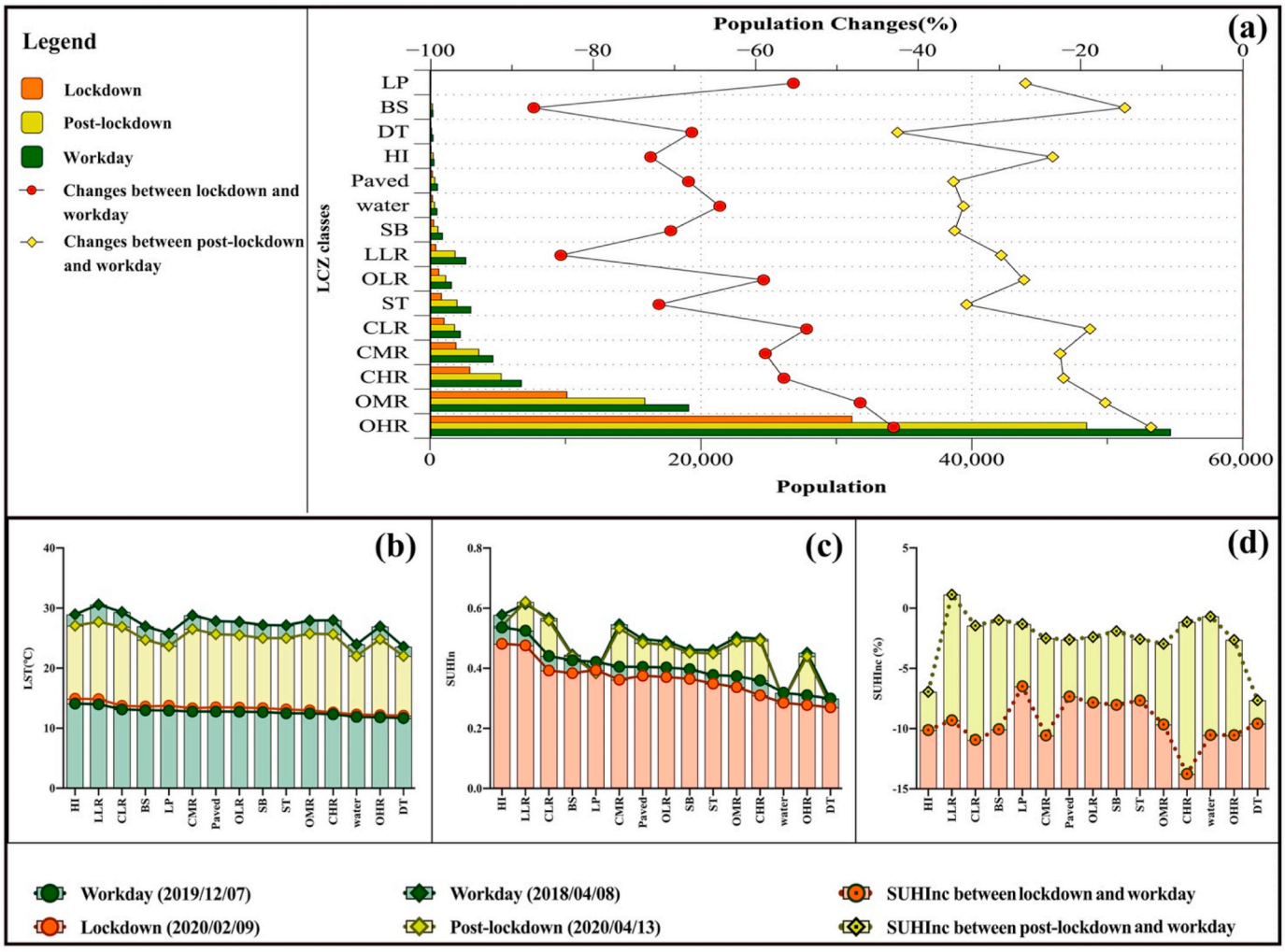


Fig. 8. Population distribution in different LCZ classes and its associated changes after city lockdown (a) and LST (b), SUHIn (c) and SUHInc (d) in various LCZ classes.

(−9.66%), LLR (−9.31%), SB (−8.03%), OLR (−7.84%), ST (−7.66%) and LP (−6.49%) (Fig. 8d). The population changes and $SUHI_{nc}$ between the post-lockdown and workday periods almost remained the same trend, and their differences almost disappear after the return of residents and outdoor activities to Wuhan City (Fig. 8d).

4.3. Correlations between PD and LST

In this study, we found that the PD has a significant negative relationship with LST in several types of urban land uses, especially in the urban construction land (Fig. 7a and b). Actually, the population distribution is uneven, with most populations located on residential land with a lower LST and fewer residents located on industrial land or commercial areas with a higher LST (Fig. 9). This distribution can result

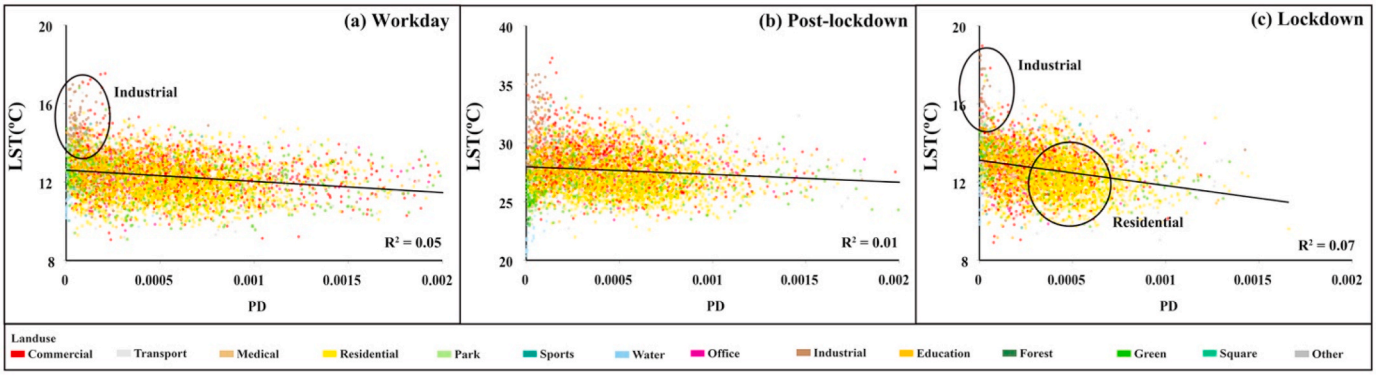


Fig. 9. Scatter plots between PD and LST with urban land use information on workdays (a), post-lockdown (b) and lockdown periods (c).

in a negative relationship between PD and LST at the city level. Since the city lockdown, many workers in industrial land or commercial areas have returned to their homes and the populations are concentrated on residential land (Fig. 9c). These changes can enlarge the uneven distribution of the population and may lead to more significant correlations between PD and LST in the lockdown period, with this correlation increasing from −0.215** (workday) to −0.257** (lockdown) at the city level.

Similarly, the population and LST distribution were also uneven in the same type of urban land use. On industrial land, most populations were located in the OMR class with a lower LST and only few populations were located in the LLR class with a higher LST (Fig. 10b). Since the city lockdown, the decreased population are mainly in LLR classes (Figs. 10b-1), which decreased the negative correlations between PD and LST. On residential land, the dense population was located in the OHR class with a lower LST and the sparse population was located in the CLR class with a higher LST (Fig. 10e). This change can produce a significant negative correlation between PD and LST. Since the city lockdown, the residents moved out of the city centre in the CHR class and were concentrated in the OHR class (Figs. 10e-1), which could intensify the negative relationship between PD and LST. The different urban morphologies did not impact the medical (Fig. 10f) and office lands (Fig. 10d), which were dominated by one LCZ class. The impact of the population and its anthropogenic heat release on the urban thermal environment can produce a weaker positive relationship between PD and LST in those areas.

4.4. Limitations and future studies

In this study, due to the limitations in remote sensing images in terms of accessibility and issues associated with various weather conditions, only four remote sensing images were applied and used to retrieve the LST. The LST was then used to represent the thermal environment index and analyze the impact of population changes and human activities on the urban thermal environment. Considering a greater number of cities and comparing their thermal changes could lead to more reliable results. Moreover, by using the air temperature, we may obtain better results because anthropogenic heat is directly released to the air; thus, using LST may underestimate its impact. Even though we selected the days under similar weather conditions for comparison. However, it can not totally eliminate the weather differences on the impact of the urban thermal environment, such as wind speed or solar radiation on a small land block area. Conducting a research combined with climate models and situ measurement and comparing them can make the results more reliable. Active users on an online platform were analysed for the population data, and these values are not representative of the whole population; thus, the population size may have been underestimated. Combining online data with other data sources, such as census data and mobile signalling data, can improve the accuracy. We use the acquired population numbers in various urban land uses as an index to reflect the change in human activities. Actually, different human activities have different levels of energy consumption; for example, manufacturing activities may consume more energy than residential activities [61]. Therefore, converting the population numbers to anthropogenic heat release and considering their differences may yield better results.

Moreover, the urban thermal environment is combined with many

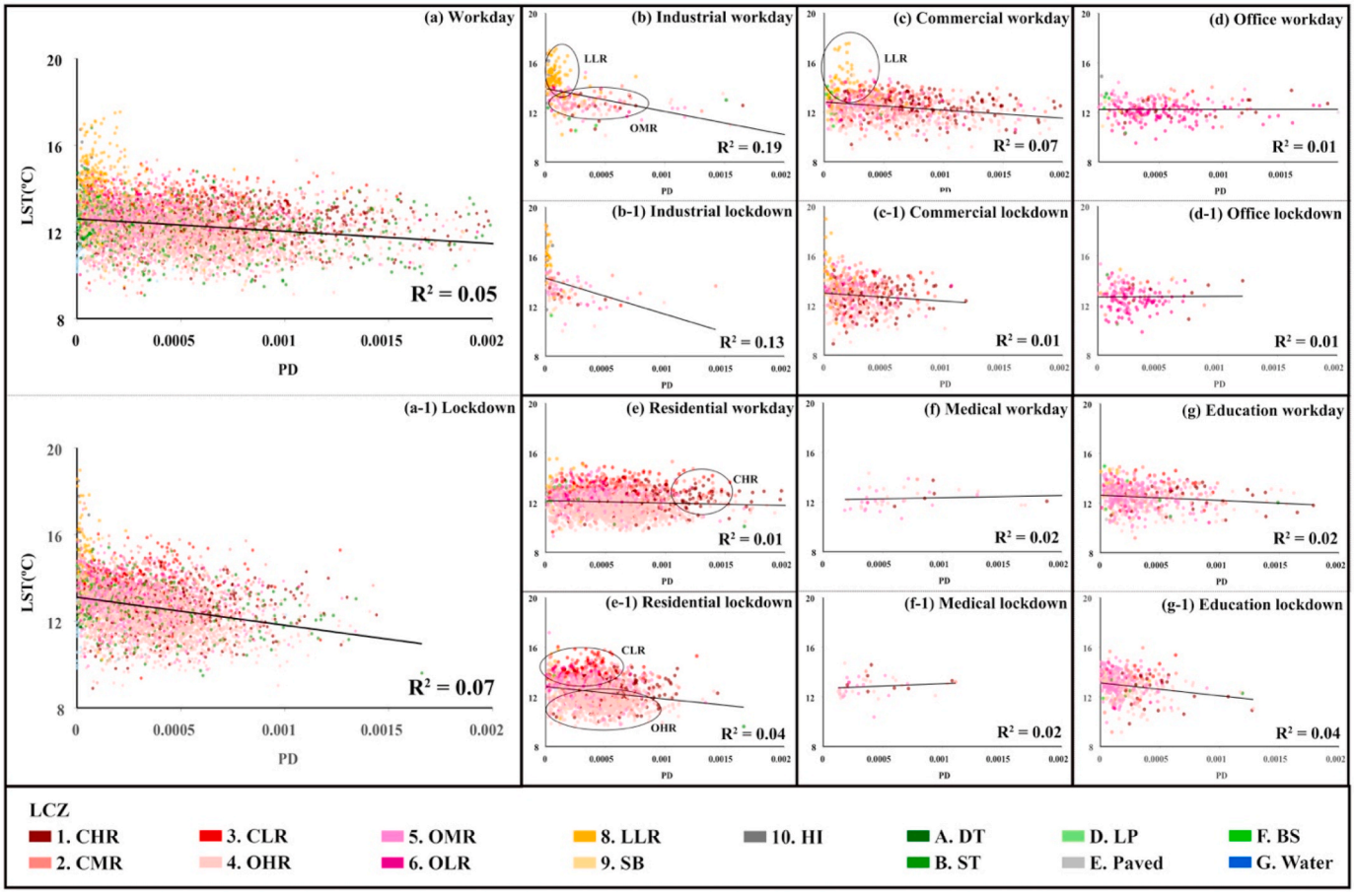


Fig. 10. Scatter plots between PD and LST with LCZ class information on workdays (a) and lockdown periods (a-1); scatter plots between PD and LST for various urban land uses with LCZ class information (b–g).

factors that may play an important role in the spatial-temporal distribution of LST. For example, land cover and urban morphology were found to have effects in this study and green spaces and water bodies were found to have cooling effects in other studies and thus play important roles [12]. Therefore, it is necessary to conduct more studies to compare the influence of such interactions. The use of nighttime LST data may also reduce the impact of solar radiation on the relationship between anthropogenic heat release and the urban thermal environment [36,62].

5. Conclusions

In this study, we compared the population changes and thermal environment differences before and after city lockdown from the perspective of urban land use and the LCZ. The results show that COVID-19 reduced human activities. Combined with the Spring Festival, the population decreased significantly in industrial and commercial land, and larger thermal differences also appeared in those land and LCZ built-up classes.

The population changes did not modify the spatial distribution of the thermal environment but reduced the thermal differences in different land use and LCZ classes. As the LST showed the same trend in various land use and LCZ classes before and after the city lockdown, and the normalized surface urban heat island ($SUHI_n$) decreased in all urban land use and LCZ classes during the lockdown. The OLS model showed that the thermal differences were mainly caused by changes in population size and human activities under similar weather conditions. The model also illustrated that the contribution of the population and its anthropogenic heat release to the urban thermal environment is relatively weak, solar radiation and urban morphology play a more critical role in the urban thermal environment.

The above findings enlighten us that urban planners and policy-makers should pay more attention to areas with a dense population and worse thermal environment, and apply different methods to reduce the impact of urban heat island for various urban land uses and LCZ classes. For example, moving the heavy industry factories out of the city centre, changing the LLR class of light industrial buildings to the OMR class, integrating heat impact assessments and heat warning systems into public health practice in residential areas. Thus, alleviate the urban heat island effect and making cities cope with climate change.

Declaration of competing interest

The authors declare that they have no known competing financial interests or personal relationships that could have appeared to influence the work reported in this paper.

Acknowledgments

This work was supported by the National Natural Science Foundation of China (Grant No. 51978363 and 51878515), Beijing Social Science-Foundation (Grant No. 19GLB034) and National Key Research and Development Program of China (Grant No. 2018YFC0704600), Beijing Key Laboratory of Spatial Development for Capital Region (Grant No. 20202000919).

Appendix A

Table 1
Values of different index properties for LCZ classes.

LCZ	Sky View Factor	Aspect Ratio	Building Surface Fraction (%)	Impervious Surface Fraction (%)	Pervious Surface Fraction (%)	Height of Roughness Elements (m)	Terrain Roughness Class	Surface Admittance (J $m^{-2}s^{-1/2}K^{-1}$)	Surface Albedo	Anthropogenic Heat Output (W m^{-2})
LCZ 1 Compact high-rise (CHR)	0.2–0.4	>2	40–60	40–60	<10	>25	8	1500–1800	0.10–0.20	50–300
LCZ 2 Compact mid-rise (CMR)	0.3–0.6	0.75–2	40–70	30–50	<20	10–25	6–7	1500–2200	0.10–0.20	<75
LCZ 3 Compact low-rise (CLR)	0.2–0.6	0.75–1.5	40–70	20–50	<30	3–10	6	1200–1800	0.10–0.20	<75
LCZ 4 Open high-rise (OHR)	0.5–0.7	0.75–1.25	20–40	30–40	30–40	>25	7–8	1400–1800	0.12–0.25	<50
LCZ 5 Open mid-rise (OMR)	0.5–0.8	0.3–0.75	20–40	30–50	20–40	10–25	5–6	1400–2000	0.12–0.25	<25
LCZ 6 Open low-rise (OLR)	0.6–0.9	0.3–0.75	20–40	20–50	30–60	3–10	5–6	1200–1800	0.12–0.25	<25
LCZ 8 Large low-rise (LLR)	>0.7	0.1–0.3	10–20	40–50	<20	3–10	5	1200–1800	0.15–0.25	<50
LCZ 9 Sparsely built (SB)	>0.8	0.1–0.25	20–30	<20	60–80	3–10	5–6	1000–1800	0.12–0.25	<10
LCZ 10 Heavy industry (HI)	0.6–0.9	0.2–0.5	<10	20–40	40–50	5–15	5–6	1000–2500	0.12–0.20	0
LCZ A Dense trees (DT)	<0.4	>1	<10	<10	>90	3–30	8	–	0.10–0.20	0

(*continued on next page*)

Table 1 (*continued*)

LCZ	Sky View Factor	Aspect Ratio	Building Surface Fraction (%)	Impervious Surface Fraction (%)	Pervious Surface Fraction (%)	Height of Roughness Elements (m)	Terrain Roughness Class	Surface Admittance (J $m^{-2}s^{-1/2}K^{-1}$)	Surface Albedo	Anthropogenic Heat Output (W m^{-2})
LCZ B Scattered trees (ST)	0.5–0.8	0.25–0.75	<10	<10	>90	3–15	5–6	700–1500	0.15–0.25	0
Lcz C Bush, scrub (BS)	0.7–0.9	0.25–1.0	<10	<10	>90	<2	4–5	1200–1600	0.15–0.25	0
LCZ D Low plants (LP)	>0.9	<0.1	<10	<10	>90	<1	3–4	1200–2500	0.15–0.30	0
LCZ E Bare rock or paved (Paved)	>0.9	<0.1	<10	>90	<10	<0.25	1–2	600–1400	0.20–0.35	0
LCZ F Bare soil or sand (BSS)	>0.9	<0.1	<10	<10	>90	<0.25	1–2	600–1400	0.20–0.35	0
LCZ G Water	>0.9	<0.1	<10	<10	>90	–	1	1500	0.02–0.10	0

References

[1] M. de Haas, R. Faber, M. Hamersma, How COVID-19 and the Dutch 'intelligent lockdown' change activities, work and travel behaviour: evidence from longitudinal data in The Netherlands, Transport. Resear. Interdiscipl. Perspect. (2020) 100150.

[2] The Earth Institute, Columbia University, New Data Suggest COVID-19 Is Shifting the Burden of Energy Costs to Households, 2020, April 21. Retrieved June 1, 2020, from, https://blogs.ei.columbia.edu/2020/04/21/covid-19energy-costs-households/.

[3] C. Le Quéré, R.B. Jackson, M.W. Jones, A.J. Smith, S. Abernethy, R.M. Andrew, P. Friedlingstein, Temporary reduction in daily global CO_2 emissions during the COVID-19 forced confinement, Nat. Clim. Change (2020) 1–7.

[4] A.K. Quah, M. Roth, Diurnal and weekly variation of anthropogenic heat emissions in a tropical city, Singapore, Atmos. Environ. 46 (2012) 92–103.

[5] M.K. Firozjaei, Q. Weng, C. Zhao, M. Kiavarz, L. Lu, S.K. Alavipanah, Surface anthropogenic heat islands in six megacities: an assessment based on a triple-source surface energy balance model, Remote Sens. Environ. 242 (2020) 111751.

[6] V. Masson, A physically-based scheme for the urban energy budget in atmospheric models, Boundary-Layer Meteorol. 94 (3) (2000) 357–397.

[7] F. Wang, H. Liu, J. Gou, W. Ding, Spatio-temporal changes of anthropogenic heat release and its impact on land surface energy balance over China, China Environ. Sci. 39 (3) (2019) 980–987 (In Chinese).

[8] Y. Zheng, Q. Weng, High spatial-and temporal-resolution anthropogenic heat discharge estimation in Los Angeles County, California, J. Environ. Manag. 206 (2018) 1274–1286.

[9] S.I. Bohnenstengel, I. Hamilton, M. Davies, S.E. Belcher, Impact of anthropogenic heat emissions on London's temperatures, Q. J. R. Meteorol. Soc. 140 (679) (2014) 687–698.

[10] H. Fan, D.J. Sailor, Modeling the impacts of anthropogenic heating on the urban climate of Philadelphia: a comparison of implementations in two PBL schemes, Atmos. Environ. 39 (1) (2005) 73–84.

[11] R. Giridharan, R. Emmanuel, The impact of urban compactness, comfort strategies and energy consumption on tropical urban heat island intensity: a review, Sustain. Cities Soc. 40 (2018) 677–687.

[12] G. Manoli, S. Fatichi, M. Schläpfer, K. Yu, T.W. Crowther, N. Meili, E. Bou-Zeid, Magnitude of urban heat islands largely explained by climate and population, Nature 573 (7772) (2019) 55–60.

[13] Z. Cai, G. Han, M. Chen, Do water bodies play an important role in the relationship between urban form and land surface temperature? Sustain. Cities Soc. 39 (2018) 487–498.

[14] Y. Liu, J. Peng, Y. Wang, Efficiency of landscape metrics characterizing urban land surface temperature, Landsc. Urban Plann. 180 (2018) 36–53.

[15] Y. Wang, Q. Zhan, W. Ouyang, How to quantify the relationship between spatial distribution of urban water bodies and land surface temperature? Sci. Total Environ. 671 (2019) 1–9.

[16] C. Fabiani, A.L. Pisello, E. Bou-Zeid, J. Yang, F. Cotana, Adaptive measures for mitigating urban heat islands: the potential of thermochromic materials to control roofing energy balance, Appl. Energy 247 (2019) 155–170.

[17] G.F. Han, Z. Cai, Y.S. Xie, W. Zeng, Correlation between urban construction and urban heat island: a case study in Kaizhou District, Chongqing, J. Civ. Arch. Env. Eng. 38 (2016) 138–147 (In Chinese).

[18] A. Mohajerani, J. Bakaric, T. Jeffrey-Bailey, The urban heat island effect, its causes, and mitigation, with reference to the thermal properties of asphalt concrete, J. Environ. Manag. 197 (2017) 522–538.

[19] A. Aflaki, M. Mirnezhad, A. Ghaffarianhoseini, A. Ghaffarianhoseini, H. Omrany, Z. H. Wang, H. Akbari, Urban heat island mitigation strategies: a state-of-the-art review on Kuala Lumpur, Singapore and Hong Kong, Cities 62 (2017) 131–145.

[20] P. Boehme, M. Berger, T. Massier, Estimating the building based energy consumption as an anthropogenic contribution to urban heat islands, Sustain. Cities Soc. 19 (2015) 373–384.

[21] Z. Cai, Y. Tang, K. Chen, G. Han, Assessing the heat vulnerability of different local climate zones in the old areas of a Chinese megacity, Sustainability 11 (7) (2019) 2032.

[22] Y. Feng, S. Du, S.W. Myint, M. Shu, Do urban functional zones affect land surface temperature differently? A case study of Beijing, China, Rem. Sens. 11 (15) (2019) 1802.

[23] R. Sun, Y. Lü, X. Yang, L. Chen, Understanding the variability of urban heat islands from local background climate and urbanization, J. Clean. Prod. 208 (2019) 743–752.

[24] D. Lai, W. Liu, T. Gan, K. Liu, Q. Chen, A review of mitigating strategies to improve the thermal environment and thermal comfort in urban outdoor spaces, Sci. Total Environ. 661 (2019) 337–353.

[25] Y. Zhang, A.T. Murray, B.L. Turner Ii, Optimizing green space locations to reduce daytime and nighttime urban heat island effects in Phoenix, Arizona, Landsc. Urban Plann. 165 (2017) 162–171.

[26] E.M. Chibuike, A.O. Ibukun, A. Abbas, J.J. Kunda, Assessment of green parks cooling effect on Abuja urban microclimate using geospatial techniques, Rem. Sens. Appl.: Soc. Environ. 11 (2018) 11–21.

[27] Z. Yu, G. Yang, S. Zuo, G. Jørgensen, M. Koga, H. Vejre, Critical review on the cooling effect of urban blue-green space: a threshold-size perspective, Urban For. Urban Green. (2020) 126630.

[28] J. Natanian, O. Aleksandrowicz, T. Auer, A parametric approach to optimizing urban form, energy balance and environmental quality: the case of Mediterranean districts, Appl. Energy 254 (2019) 113637.

[29] A. Aboelata, Vegetation in different street orientations of aspect ratio (H/W 1: 1) to mitigate UHI and reduce buildings' energy in arid climate, Build. Environ. 172 (2020) 106712.

[30] I.D. Stewart, T.R. Oke, Local climate zones for urban temperature studies, Bull. Am. Meteorol. Soc. 93 (12) (2012) 1879–1900.

[31] O. Brousse, S. Georganos, M. Demuzere, S. Vanhuysse, H. Wouters, E. Wolff, S. Dujardin, Using local climate zones in Sub-Saharan Africa to tackle urban health issues, Urban Clim. 27 (2019) 227–242.

[32] Y. Wu, A. Sharifi, P. Yang, H. Borjigin, D. Murakami, Y. Yamagata, Mapping building carbon emissions within local climate zones in Shanghai, Energy Procedia 152 (2018) 815–822.

[33] R. Kotharkar, A. Ramesh, A. Bagade, Urban heat island studies in south asia: a critical review, Urban Clim. 24 (2018) 1011–1026.

[34] K. Deilami, M. Kamruzzaman, Y. Liu, Urban heat island effect: a systematic review of spatio-temporal factors, data, methods, and mitigation measures, Int. J. Appl. Earth Obs. Geoinf. 67 (2018) 30–42.

[35] C. He, L. Zhou, Y. Yao, W. Ma, P.L. Kinney, Estimating temporal-spatial effects of anthropogenic heat emissions upon the urban thermal environment in an urban agglomeration area in East China, Sustain. Cities Soc. (2020) 102046.

[36] M. Parsaee, M.M. Joybari, P.A. Mirzaei, F. Haghighat, Urban heat island, urban climate maps and urban development policies and action plans, Environ. Technol. Innov. (2019) 100341.

[37] M.L. Lambert-Habib, J. Hidalgo, C. Fedele, A. Lemonsu, C. Bernard, How is climatic adaptation taken into account by legal tools? Introduction of water and vegetation by French town planning documents, Urban Clim. 4 (2013) 16–34.

[38] C. He, L. Ma, L. Zhou, H. Kan, Y. Zhang, W. Ma, B. Chen, Exploring the mechanisms of heat wave vulnerability at the urban scale based on the application of big data and artificial societies, Environ. Int. 127 (2019) 573–583.
[39] T. Shelton, A. Poorthuis, M. Graham, M. Zook, Mapping the data shadows of Hurricane Sandy: uncovering the sociospatial dimensions of 'big data, Geoforum 52 (2014) 167–179.
[40] D.J. Sailor, A review of methods for estimating anthropogenic heat and moisture emissions in the urban environment, Int. J. Climatol. 31 (2) (2011) 189–199.
[41] N. Girgis, S. Elariane, M.A. Elrazik, Evaluation of heat exhausts impacts on pedestrian thermal comfort, Sustain. Cities Soc. 27 (2016) 152–159.
[42] Z. Cao, Z. Wu, L. Liu, Y. Chen, Y. Zou, Assessing the relationship between anthropogenic heat release warming and building characteristics in Guangzhou: a sustainable development perspective, Sci. Total Environ. 695 (2019) 133759.
[43] W. Liu, W. Wu, P. Thakuriah, J. Wang, The geography of human activity and land use: a big data approach, Cities 97 (2020) 102523.
[44] X. Yang, Z. Fang, L. Yin, J. Li, S. Lu, Z. Zhao, Revealing the relationship of human convergence–divergence patterns and land use: a case study on Shenzhen City, China, Cities 95 (2019) 102384.
[45] T.J.J. Wuhan, GOV.CN. Statistical Bulletin of Wuhan National Economic and Social Development in 2019, 2020 available at: http://tjj.wuhan.gov.cn/tjfw/tjgb/202004/t20200429_1191417.shtml.
[46] The State Council Information Office of the People's Republic of China, Fighting covid-19 China in action, available at: http://www.scio.gov.cn/zfbps/ndhf/42312/Document/1682142/1682142.htm, 2020.
[47] C. Li, F. Li, Z. Wu, J. Cheng, Exploring spatially varying and scale-dependent relationships between soil contamination and landscape patterns using geographically weighted regression, Appl. Geogr. 82 (2017) 101–114.
[48] M. Masoudi, P.Y. Tan, Multi-year comparison of the effects of spatial pattern of urban green spaces on urban land surface temperature, Landsc. Urban Plann. 184 (2019) 44–58.
[49] M.N. Peiró, C.S.G. Sánchez, F.N. González, Source area definition for local climate zones studies. A systematic review, Build. Environ. 148 (2019) 258–285.
[50] B. Bechtel, M. Demuzere, G. Mills, W. Zhan, P. Sismanidis, C. Small, J. Voogt, SUHI analysis using Local Climate Zones—a comparison of 50 cities, Urban Clim. 28 (2019) 100451.
[51] A. Sekertekin, S. Bonafoni, Land surface temperature retrieval from landsat 5, 7, and 8 over rural areas: assessment of different retrieval algorithms and emissivity models and toolbox implementation, Rem. Sens. 12 (2) (2020) 294.
[52] D. Skoković, J.A. Sobrino, J.C. Jimenez-Munoz, G. Soria, Y. Julien, C. Mattar, J. Cristóbal, Calibration and Validation of Land Surface Temperature for Landsat8-TIRS Sensor. Land Product Validation and Evolution, 2014.
[53] C. Wang, R. Pan, X. Wan, Y. Tan, L. Xu, C.S. Ho, R.C. Ho, Immediate psychological responses and associated factors during the initial stage of the 2019 coronavirus disease (COVID-19) epidemic among the general population in China, Int. J. Environ. Res. Publ. Health 17 (5) (2020) 1729.
[54] J. Li, G. Xu, Lessons from the experience in Wuhan to reduce risk of COVID-19 infection in patients undergoing long-term hemodialysis, Clin. J. Am. Soc. Nephrol. 15 (5) (2020) 717–719.
[55] H. Mei, X. Dong, Y. Wang, L. Tang, Y. Hu, Managing patients with cancer during the COVID-19 pandemic: frontline experience from Wuhan. The Lancet, Oncology 21 (5) (2020) 634.
[56] O. Rotem-Mindali, Y. Michael, D. Helman, I.M. Lensky, The role of local land-use on the urban heat island effect of Tel Aviv as assessed from satellite remote sensing, Appl. Geogr. 56 (2015) 145–153.
[57] S. Guha, H. Govil, A. Dey, N. Gill, Analytical study of land surface temperature with NDVI and NDBI using Landsat 8 OLI and TIRS data in Florence and Naples city, Italy, European J. Rem. Sens. 51 (1) (2018) 667–678.
[58] X. Chen, Y. Zhang, Impacts of urban surface characteristics on spatiotemporal pattern of land surface temperature in Kunming of China, Sustain. Cities Soc. 32 (2017) 87–99.
[59] B. Chen, C. Wu, X. Liu, L. Chen, J. Wu, H. Yang, H.Y. Brown, Seasonal climatic effects and feedbacks of anthropogenic heat release due to global energy consumption with CAM5, Clim. Dynam. 52 (11) (2019) 6377–6390.
[60] P. Du, J. Chen, X. Bai, W. Han, Understanding the seasonal variations of land surface temperature in Nanjing urban area based on local climate zone, Urban Clim. 33 (2020) 100657.
[61] S. Chen, D. Hu, M.S. Wong, H. Ren, S. Cao, C. Yu, H.C. Ho, Characterizing spatiotemporal dynamics of anthropogenic heat fluxes: a 20-year case study in Beijing–Tianjin–Hebei region in China, Environ. Pollut. 249 (2019) 923–931.
[62] D. Narumi, A. Kondo, Y. Shimoda, Effects of anthropogenic heat release upon the urban climate in a Japanese megacity, Environ. Res. 109 (4) (2009) 421–431.